A Methodology for Parameter Estimation of Nonlinear Single Track Models from Multibody Full Vehicle Simulation

2020-xx-xxxx

A methodology for parameter estimation of nonlinear single track models from multibody full vehicle simulation

Author, co-author (Do NOT enter this information. It will be pulled from participant tab in MyTechZone)

Affiliation (Do NOT enter this information. It will be pulled from participant tab in MyTechZone)

Abstract

In vehicle dynamics, simple and fast vehicle models are required, especially in the framework of real-time simulations and autonomous driving software. Therefore, a trade-off between accuracy and simulation speed must be pursued by selecting the appropriate level of detail and the corresponding simplifying assumptions based on the specific purpose of the simulation. The aim of this study is to develop a methodology for map and parameter estimation from multibody simulation results, to be used for simplified vehicle modelling focused on handling performance. In this paper, maneuvers, algorithms and results of the parameter estimation are reported, together with their integration in single track models with increasing complexity and fidelity. The agreement between the multibody model, used as reference, and four single track models is analyzed and discussed through the evaluation of the correlation index. The good match between the models validates the adopted simulation methodology both during steady-state and during transient maneuvers. In a similar way, this method could be applied to experimental data gathered from a real instrumented car rather than from a multibody model.

Introduction

The ability to predict the vehicle dynamic behavior as the design parameters change is particularly important throughout the development phases of a car. In this regard, in order to reduce calculation, design and verification times, the investigation of simulation solutions with low computational cost is very important. However, even in the early design phases it is necessary to use models that can faithfully reproduce the dynamics of the vehicle both in steady-state and transient conditions [1]. This behavior of the vehicle is strongly influenced by the physical characteristics of the tires as well as suspensions kinematics, compliances and damping [2]. In addition, modeling vehicle response delays is fundamental for dynamic simulations [3].

In this regard, this paper aims at deriving, from a detailed multibody model, a set of faster single track models with increasing complexity and fidelity [4]. The post-processing of multibody simulation results data and the implementation of the bicycle models are performed in Matlab/Simulink. The inputs of these simplified models are the vehicle speed and steering wheel angle and the outputs are COG (center of gravity) lateral velocity, lateral acceleration, yaw rate, front and rear sideslip angles. The reference maneuver for the steady-state cornering behavior characterization and comparison is the ramp steer. This maneuver consists of running a spiral trajectory at constant speed (Cruise Control active) until the vehicle loses grip. This test refers to the ISO 4138:2004 [5] and it was used in order to examine the lateral steady-state dynamic behaviour of the vehicle and for the evaluation of the nonlinear lateral force vs sideslip angle characteristic of the axles. These maps can be directly obtained from the multibody simulation results data, but can be extracted from experimental data acquisitions as well by using dedicated sensors or estimators (i.e. for vehicle side-slip angle [6-7]). Furthermore, mean roll stiffness and roll damping values are estimated from elastic and dissipative suspension components look-up tables and finally their elastic and dissipative effects are compared during steady-state and transient cornering maneuvers with the multibody ones. As for the frequency response functions (FRFs) investigation, a sine sweep maneuver [8] has been adopted to excite the vehicle in the frequency range of interest. Through this maneuver, the FRF [9] between the axle sideslip angle and the corresponding lateral force, namely $\boldsymbol{F_y/\alpha}$, is acquired from multibody model and used to identify the most appropriate relaxation lengths for the two axles [10]. In addition, the sine sweep simulation was used to tune and validate the roll damping parameter.

The map identification and parameter estimation process from Adams/Car simulation results is introduced and explained in detail in the *Methodology section*. In particular, COG position, axles characteristics (cornering stiffness and relaxation length), steering ratio, roll stiffness and roll damping are evaluated. Moreover, the vehicle models proposed for benchmarking are briefly outlined. In the *Result and Discussion* section the steady-state and frequency response functions of the various models are analyzed and compared with respect to the multibody simulations. A detailed investigation about the improvement in model accuracy associated with the increase of the model complexity is provided and assessed through the usage of the correlation index [11]. Finally, the most accurate single track model (with nonlinear cornering stiffness, relaxation length and roll motion) has been tested under different vehicle setup (i.e. mass, velocity, static toe, anti-roll bars stiffness) to prove the effectiveness of the whole procedure and the accuracy of the results for handling performance assessment.

Methodology

In this section, the methodology for the acquisition of the main vehicle characteristics from a multibody model is explained. In addition, the vehicle models used are fully described.

Tested Vehicle

The Multibody Adams/Car model (which will be referred to as *MB model* in the following) considered in this study is an all-wheel-drive (AWD) D-segment sedan with front and rear open differentials, see Figure 1. The front suspension is a Macpherson, while the rear one is a multilink. In Figure 2 the front and rear suspension assemblies of the sedan are shown. The MB model, having 56 degrees of freedom, is evidently much more detailed and complex if compared with a single track model and requires many data to setup a simulation. The sedan has the following characteristics, defined in Table 1:

TABLE 1 Main vehicle characteristics

Variable	Symbol	Unit	Value
Total mass	m	kg	1854
Sprung mass	m_s	kg	1661
Wheelbase	L	m	2.72
Distance of car COG from the front axle	a	m	1.14
Distance of car COG from the rear axle	b	m	1.58
Track width	t	m	1.55
COG height	h	m	0.49
Yaw inertia	J_z	kg m^2	2193
Mean steering ratio	R_s	-	17
Roll stiffness	k_ϕ	kNm/rad	155
Roll damping	c_ϕ	kNms/rad	6.18
Tire size	R_0	-	235/40 R18

The Pacejka tire model is used for handling simulations of the multibody vehicle, in the version PAC2002. The “use mode” selected for Adams/Car simulations is the most complex one considering the combined force/moment calculation and the relaxation behavior.

FIGURE 1 A global view of the multibody model

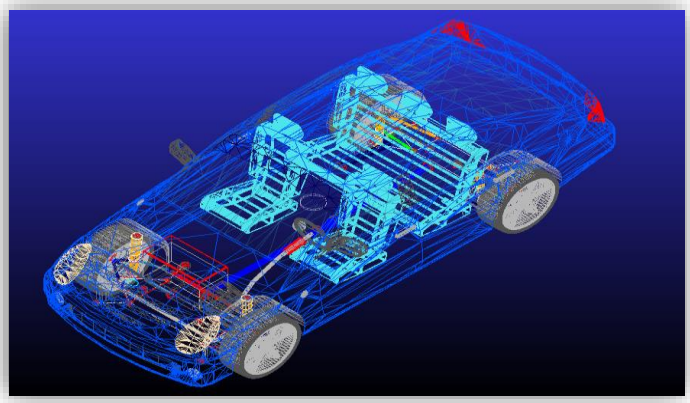

FIGURE 2 Front (MacPherson) and rear (multilink) suspension

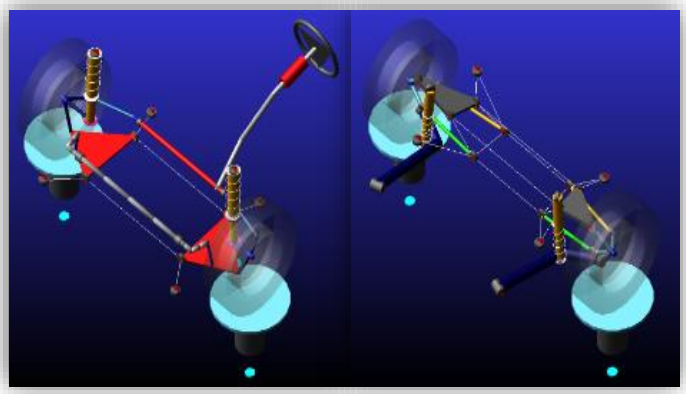

Vehicle Models

Table 2 lists and compares the selected four single track models (which will be referred to as *ST models* in the following) whose parameters will be estimated by the proposed methodology. These models are widely used for vehicle lateral dynamics simulations. Model 1 is the classical ST model with constant parameters (a typical LTI dynamic system) without tire delay, Model 2 introduces the tire delay through a first order relaxation length model between axle sideslip angle and actual lateral force. Model 3 adds the nonlinearity of the cornering behavior of the two axles and Model 4 further increases the realism of the model by modelling the roll motion of the chassis. The mathematical description of Models 1 and 2 can be easily found in the Literature, see e.g. [4]; model 3 and 4 will be analyzed in detail in the following paragraphs. It must be noticed that vehicle velocity is assumed constant during simulation for all the analyzed models.

TABLE 2 The selected single track vehicle models

Model Name	Rel. Length	Cornering stiffness	Roll
Model 1	✗	*Constant*	✗
Model 2	✓	*Constant*	✗
Model 3	✓	Variable with α	✗
Model 4	✓	Variable with α	✓

Model 3 - ST model with nonlinear steady-state axles characteristics and constant relaxation lengths

Model 3 extends the validity of the single track model over a wider lateral acceleration range than the classical model with constant cornering stiffness, i.e. Model 1. The axles characteristics are imported in the model as 1D map as a function of the axle sideslip angle α, the latter being evaluated as the mean value of the sideslip angles of the wheels belonging to the same axle. The equations of motion can be easily derived starting from the dynamic equilibrium equations of the vehicles and assuming first-order lags, based on a constant relaxation length model, for the transient force generation of the axles:

$$\begin{cases} m\left(\dot{v} + u\dot{\psi}\right) = F_{y,f} + F_{y,r} \\ J_z\ddot{\psi} = aF_{y,f} - bF_{y,r} \\ \frac{d_f}{u}\dot{F}_{y,f} + F_{y,f} = F_{y,f,ss}(\alpha) \\ \frac{d_r}{u}\dot{F}_{y,r} + F_{y,r} = F_{y,r,ss}(\alpha) \end{cases} \quad (1)$$

where:

$\dot{\psi}$	Yaw rate
$\ddot{\psi}$	Yaw acceleration
$d_{f/r}$	Relaxation length front/rear
$F_{y,f/r}$	Lateral force front/rear
$F_{y,f/r,ss}$	Steady-state lateral force front/rear
u	Longitudinal vehicle velocity
v	Lateral vehicle velocity

In Figure 3 the nonlinear trends of the axles cornering force (bottom) and the steering ratio (top) are shown. A variable steering ratio R_s as a function of the steering-wheel angle δ_{vol} is implemented in Simulink through a 1D look-up table; the steady-state axle lateral forces $F_{y,f,ss}(\alpha)$ and $F_{y,r,ss}(\alpha)$ are modelled as non-linear functions of axle side slip angles also implemented through a 1D look-up table. The steering ratio map $R_s(\delta_{sw})$ affects the conversion from the angle applied by the driver to the steering wheel δ_{sw} to the front wheels steer angle δ_w.

FIGURE 3 Maps of the steering ratio (top), axle cornering force (bottom left) and axle cornering stiffness (bottom right), as used in Model 3.

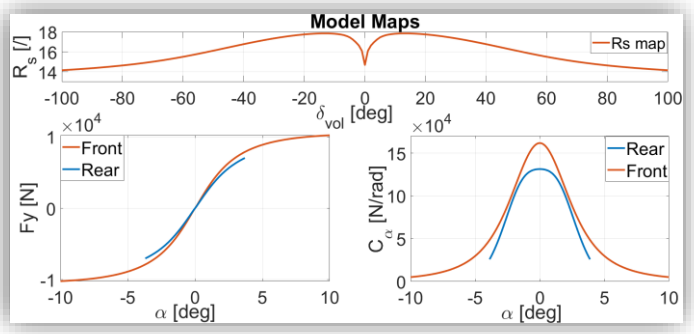

To study the dynamic behavior of the vehicle in a neighborhood of a generic equilibrium point characterized by a constant side slip angle α_0, e.g. for stability analysis purposes, the axles steady-state characteristics can be linearized as follows:

$$F_{y,ss}(\alpha) = F_y(\alpha_0) + C_\alpha(\alpha_0)(\alpha - \alpha_0) = F_{y0} + C_0(\alpha - \alpha_0) \tag{2}$$

Where:

α	Side slip angle
α_0	Side slip angle at the linearization point
C_α	Cornering stiffness
C_0	Cornering stiffness at the linearization point
F_{y0}	Lateral force at the linearization point

Introducing linearization in the last two equations of (1) and using the kinematic equations of the single track model, the system becomes:

$$\begin{cases} \dot{\beta} = -\dot{\psi} + \frac{F_{y,f}+F_{y,r}}{mu} \\ \ddot{\psi} = \left(\frac{F_{y,f}\,a - F_{y,r}\,b}{Jz}\right) \\ \frac{d_f}{u}\dot{F}_{y,f} + F_{y,f} = -C_{f,0}\beta + \left(\frac{-C_{f,0}a}{u}\right)\dot{\psi} + C_{f,0}\delta_{sw}/R_s + F_{y,f0} - C_{f,0}\alpha_{f,0} \\ \frac{d_r}{u}\dot{F}_{y,r} + F_{y,r} = -C_{r,0}\beta + \left(\frac{C_{r,0}b}{u}\right)\dot{\psi} + F_{y,r0} - C_{r,0}\alpha_{r,0} \end{cases} \tag{3}$$

Where:

β	Vehicle side slip angle at COG
$\dot{\beta}$	Vehicle side slip angle rate
$\alpha_{f/r}$	Front/rear axle side slip angle
$C_{f,0}$	Front cornering stiffness (from map)
$C_{r,0}$	Rear cornering stiffness (from map)
$\dot{F}_y$	Lateral force rate

That can be fitted in the state-space form:

$$\begin{cases} \dot{x} = Ax + B\,u + E \\ y = Cx + D\,u \end{cases} \tag{4}$$

where the *input* is the steering wheel angle $u = \{\delta_{sw}\}$, the *state variables vector* is $x = \{\beta, \dot{\psi}, F_{y,f}, F_{y,r}\}^T$, the *output vector* is $y = \{\beta, \dot{\psi}, \alpha_f, \alpha_r\}^T$ and the *state-space matrices* are:

$$\boldsymbol{A} = \begin{bmatrix} 0 & -1 & 1/mu & 1/mu \\ 0 & 0 & a/J_Z & -b/J_Z \\ -C_{F,0}u/d_f & -C_{F,0}a/d_f & -u/d_f & 0 \\ -C_{R,0}u/d_r & C_{R,0}b/d_r & 0 & -u/d_r \end{bmatrix} \tag{5}$$

$$\boldsymbol{B} = \begin{bmatrix} 0 \\ 0 \\ \frac{C_{F,0}u}{d_f R_s} \\ 0 \end{bmatrix} \tag{6}$$

$$\boldsymbol{E} = \begin{bmatrix} 0 \\ 0 \\ \frac{u}{d_f}\left(F_{y,f0} - C_{F,0}\alpha_{F,0}\right) \\ \frac{u}{d_r}\left(F_{y,r0} - C_{R,0}\alpha_{R,0}\right) \end{bmatrix} \tag{7}$$

$$\boldsymbol{C} = \begin{bmatrix} 1 & 0 & 0 & 0 \\ 0 & 1 & 0 & 0 \\ -1 & -\frac{a}{u} & 0 & 0 \\ -1 & \frac{b}{u} & 0 & 0 \end{bmatrix} \qquad \boldsymbol{D} = \begin{bmatrix} 0 \\ 0 \\ 1 \\ 0 \end{bmatrix} \tag{8}$$

Model 4 - ST model with nonlinear steady-state axles characteristics, constant relaxation lengths and roll dynamics

The lateral vehicle dynamics including the roll motion of the vehicle body, variable cornering stiffnesses and constant relaxation lengths are modelled through the following system of equations:

$$\begin{cases} m(u\dot{\beta} + u\dot{\psi}) - m_s e\dot{p} = F_{y,f} + F_{y,r} \\ J_z\ddot{\psi} - J_{zx}\dot{p} = aF_{y,f} - bF_{y,r} \\ \frac{d_f}{u}\dot{F}_{y,f} + F_{y,f} = F_{y,f,ss}(\alpha) \\ \frac{d_r}{u}\dot{F}_{y,r} + F_{y,r} = F_{y,r,ss}(\alpha) \\ [J_x + m_s e^2]\dot{p} - J_{zx}\ddot{\psi} - m_s e(u\dot{\beta} + u\dot{\psi}) = -c_\phi p - (k_\phi - m_s g e)\phi \\ \dot{\phi} = p \end{cases} \tag{9}$$

Where

e	Distance between roll axis and vehicle COG
g	Gravitational acceleration
c_ϕ	Roll (viscous) damping
k_ϕ	Roll stiffness

$\boldsymbol{\phi, p, \dot{p}}$	Roll angle, velocity, acceleration
$\boldsymbol{J_{zx}}$	Product of inertia with respect to the x-axis (roll) and z-axis (yaw)
$\boldsymbol{J_x}$	Moment of inertia of the vehicle sprung mass with respect to the x-axis (roll)
$\boldsymbol{m}$, $\boldsymbol{m_s}$	Total vehicle mass, sprung mass

The main assumption on roll dynamics is that the roll axis is horizontal and its position relative to the unsprung mass is fixed. Furthermore, the elastic and damping properties of the suspensions are lumped through a total roll stiffness k_ϕ and a total roll damping c_ϕ respectively. After introducing the linearization of the axle characteristics (eq. 2), the final set of equations is:

$$\begin{cases} mu\dot{\beta} - m_s e\dot{p} = -mu\dot{\psi} + F_{y,f} + F_{y,r} \\ J_z\ddot{\psi} - J_{zx}\dot{p} = aF_{y,f} - bF_{y,r} \\ \frac{d_f}{u}\dot{F}_{y,f} = -C_{F,0}\beta + \left(\frac{-C_{F,0}a}{u}\right)\dot{\psi} - F_{y,f} + C_{F,0}\delta_f + F_{y,f0} - C_{F,0}\alpha_{F,0} \\ \frac{d_r}{u}\dot{F}_{y,r} = -C_{R,0}\beta + \left(\frac{C_{R,0}b}{u}\right)\dot{\psi} - F_{y,r} + F_{y,r0} - C_{R,0}\alpha_{R,0} \\ [J_x + m_s e^2]\dot{p} - J_{zx}\ddot{\psi} - m_s eu\dot{\beta} = m_s eu\dot{\psi} - c_\phi p - (k_\phi - m_s ge)\phi \\ \dot{\phi} = p \end{cases} \quad (10)$$

From eq. (10) the state-space representation of the model is derived:

$$G\dot{x} = Fx + Hu + L \quad (11)$$

By expanding the former compact expression, the elements of the matrices are made explicit:

$$\begin{bmatrix} mu & 0 & 0 & 0 & -m_s e & 0 \\ 0 & J_z & 0 & 0 & -J_{z.x} & 0 \\ 0 & 0 & \frac{d_f}{u} & 0 & 0 & 0 \\ 0 & 0 & 0 & \frac{d_r}{u} & 0 & 0 \\ -m_s eu & -J_{zx} & 0 & 0 & J_x + m_s e^2 & 0 \\ 0 & 0 & 0 & 0 & 0 & 1 \end{bmatrix} \begin{bmatrix} \dot{\beta} \\ \ddot{\psi} \\ \dot{F}_{y,f} \\ \dot{F}_{y,r} \\ \dot{p} \\ \dot{\phi} \end{bmatrix} =$$

$$\begin{bmatrix} 0 & -mu & 1 & 1 & 0 & 0 \\ 0 & 0 & a & -b & 0 & 0 \\ -C_{F,0} & \frac{-C_{F,0}a}{u} & -1 & 0 & 0 & 0 \\ -C_{R,0} & \frac{C_{R,0}b}{u} & 0 & -1 & 0 & 0 \\ 0 & m_s eu & 0 & 0 & -c_\phi & -k_\phi + m_s ge \\ 0 & 0 & 0 & 0 & 1 & 0 \end{bmatrix} \begin{bmatrix} \beta \\ \dot{\psi} \\ F_{y,f} \\ F_{y,r} \\ p \\ \phi \end{bmatrix}$$

$$+ \begin{bmatrix} 0 \\ 0 \\ C_{F,0} \\ 0 \\ 0 \\ 0 \end{bmatrix} \delta_f + \begin{bmatrix} 0 \\ 0 \\ F_{y,f0} - C_{F,0}\alpha_{F,0} \\ F_{y,r0} - C_{R,0}\alpha_{R,0} \\ 0 \\ 0 \end{bmatrix} \quad (12)$$

The selected outputs of this system are:

$$y = \begin{bmatrix} \beta \\ \dot{\psi} \\ p \\ \phi \\ \alpha_f \\ \alpha_r \end{bmatrix} = \begin{bmatrix} 1 & 0 & 0 & 0 & 0 & 0 \\ 0 & 1 & 0 & 0 & 0 & 0 \\ 0 & 0 & 0 & 0 & 1 & 0 \\ 0 & 0 & 0 & 0 & 0 & 1 \\ -1 & -\frac{a}{u} & 0 & 0 & 0 & 0 \\ -1 & \frac{b}{u} & 0 & 0 & 0 & 0 \end{bmatrix} \begin{bmatrix} \beta \\ \dot{\psi} \\ F_{y,f} \\ F_{y,r} \\ p \\ \phi \end{bmatrix} + \begin{bmatrix} 0 \\ 0 \\ 0 \\ 0 \\ 1 \\ 0 \end{bmatrix} \delta_f \quad (13)$$

It is worth underlining that, during transients, lateral acceleration a_y is directly influenced by the roll dynamics, as can be noticed by looking at its expression as a function of the states and their derivatives:

$$a_y = (\dot{\beta} + \dot{\psi})\, u - e\dot{p} \quad (14)$$

Multibody Data Processing

The simulation results of the multibody model are here analyzed and used to extract the features that are required to populate with maps and parameters the proposed single track models. This section describes a method for estimating the single characteristics of these models.

COG longitudinal position

The longitudinal position of the center of gravity is evaluated using different methods, i.e. starting from the tire vertical forces acting when the vehicle is stationary and from the lateral forces measured during a ramp steer maneuver.

1) A common way to estimate the COG longitudinal position, i.e. the distances of car COG from the front (a) and rear (b) axles, is to start from the static vertical loads (F_z), by using these equations:

$$\begin{cases} a_{st} = \frac{F_{z,rear}L}{mg} \\ b_{st} = \frac{F_{z,front}L}{mg} \end{cases} \quad (15)$$

2) A second set of equations that can be alternatively used is based on the lateral tire forces (F_y) measured during a steady-state cornering test.

$$\begin{cases} a_{F_y} = \frac{F_{y,rear}L}{ma_y} \\ b_{F_y} = \frac{F_{y,front}L}{ma_y} \end{cases} \quad (16)$$

Both yaw acceleration and pneumatic trails are assumed to be null.

3) For a more accurate evaluation of the former quantities, two additional aspects should be considered. During ramp steer there is a small but not null yaw acceleration that origins a dynamic contribution due to the inertia torque around the vertical axis. The second aspect is associated to actual application point of the lateral forces, that does not coincide with the center of the tire contact patch. Therefore, an improved version of previous equations must account for the front pneumatic trail (t_f) and the rear one (t_r). Hence, starting from the yaw moment balance about the center of the front axle:

$$ma_y a' - J_z\ddot{\psi} = LF_{y,r} \quad (17)$$

The corrected distances are:

$$\begin{cases} a' = \frac{J_z\ddot{\psi} + F_{y,r}L}{F_{y,f} + F_{y,r}} \\ b' = L - a' \end{cases} \quad (18)$$

Where:

$$\begin{cases} a' = a - t_f \\ b' = b + t_r \end{cases} \quad (19)$$

With equations 15-16-18 different ways for evaluating the longitudinal position of the COG are shown. The usage of one method rather than the others will affect the steady-state and frequency response of the vehicle. In order to monitor the ST model accuracy enhancement according to the refinement of the post processing algorithms a proper correlation index having the following mathematical expression:

$$\rho = \sqrt{\frac{\Sigma(y_{model} - \bar{y}_{multibody})^2}{\Sigma(y_{multibody} - \bar{y}_{multibody})^2}} \cdot 100 \quad (20)$$

is introduced and used to perform the assessment, being

y_{model}	ST Model data
$y_{multibody}$	MB data
$\bar{y}_{multibody}$	Mean MB data
ρ	Correlation index between ST and MB model

The correlation index values span from 0, when the two models are completely in disagreement, to 100, if the compared trends are perfectly overlapping.
Figure 5 shows the correlation index between ST *Model 4* and MB model considering the 3 proposed algorithms for the evaluation of parameters a and b. To evaluate the accuracy of ST Model during steady-state maneuvers the correlations of understeer gradient (k_{us}) and vehicle side slip angle gradient (k_β) in the whole lateral acceleration range are computed.

FIGURE 5 Model correlation during ramp steer and sine sweep tests with different method for computing the COG position.

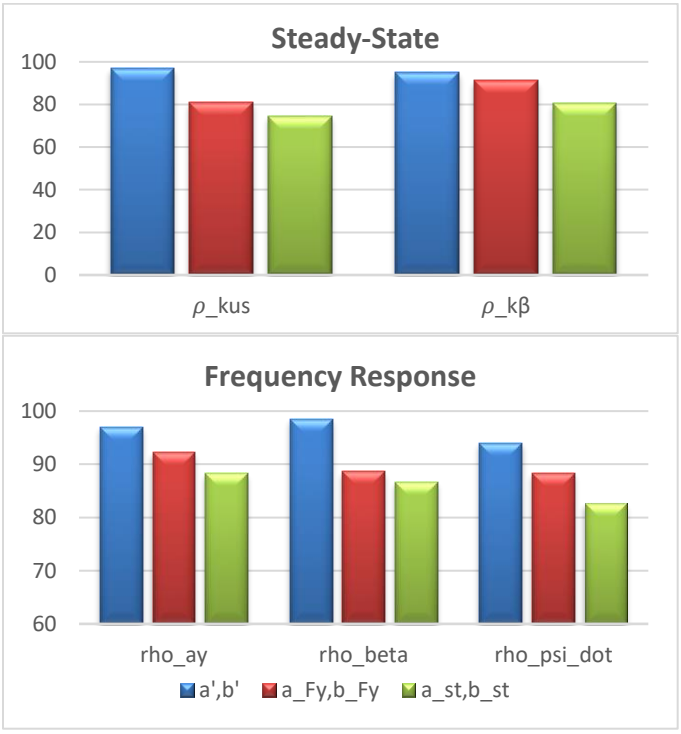

The top part of Figure 5 underlines the improvement of the steady-state simulation obtained through the usage of a corrected front and rear axles distance from the center of gravity eq. 18 (a', b' in blue) with respect the solution based only on the lateral forces eq. 16 (a_{F_y}, b_{F_y} in red). The correlation improvement is even higher if the model correlation using a' and b' (blue bar) is compared with the one with a_{st}, b_{st} (green bar) obtained from the static vertical loads. A similar improvement was also obtained during transient tests: in this case the comparison is focused on the following FRFs: $\frac{a_y}{\delta_w}$, $\frac{\beta}{\delta_w}$ and $\frac{\dot{\psi}}{\delta_w}$. The correlation indices are computed starting from the Bode diagrams of each of the aforementioned FRFs, which in turn are estimated during sweep steer test for both the ST Model 4 and the MB Model. The final value reported in the bottom part of Figure 5 is a weighted mean considering the correlation of the magnitude, the phase, and the delay of the FRFs. As for the steady-state response, the usage of the corrected values a', b' significantly improves the ST model fidelity.

FIGURE 6 Steering ratio trend as a function of the steering wheel angle, obtained from the MB model simulation during a ramp steer at 10deg/s and 90 km/h.

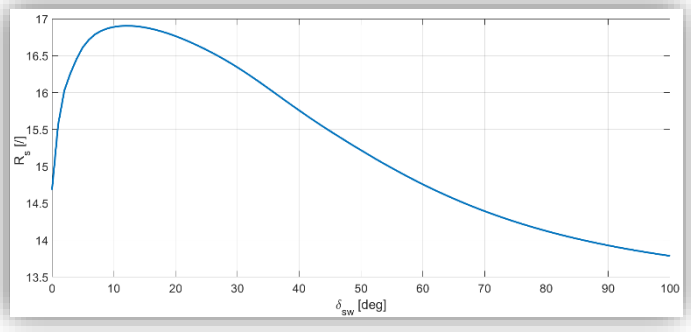

Steering Ratio

The classic single track model assumes a constant steering ratio, but the characteristic of the steering system together with the suspension kinematics and compliances actually determine a variable steering ratio, see e.g. the trend reported in Figure 6 that was obtained from a ramp steer simulation (10 deg/s and 90 km/h) of the MB model. It is worth underlining that this steering ratio map is also a function of the vehicle speed and should be identified every time the considered maneuver or its parameters change. Therefore, the MB model was upgraded to allow the computation of the front axle steering angle that is necessary to compute the variable steering ratio of the vehicle as a function of the steering wheel angle. In Adams/Car the steering ratio cannot be directly evaluated from the output of a full vehicle simulation starting from the quantity normally available in the results files. In fact, in the full vehicle simulation the steer angles of the wheels are not measured by default. Hence, it was necessary to create special virtual sensors to this aim. These sensors output the wheels toe angles by evaluating the angular position of the wheels with respect to the vehicle reference system. In this way, considering the well-known sign convention for toe angles reported in Figure 7, it was possible to calculate the steering ratio R_s of the vehicle directly from the ramp steer simulation of the complete vehicle according to the following equation:

$$R_s = \frac{\delta_{sw}}{\frac{-toe_{w,FL} + toe_{w,FR}}{2}} \quad (21)$$

Where:

δ_{sw}	Steering wheel angle
$toe_{w,FL}$	Front-left wheel toe angle
$toe_{w,FR}$	Front-right wheel toe angle

FIGURE 7 Toe angle sign convention

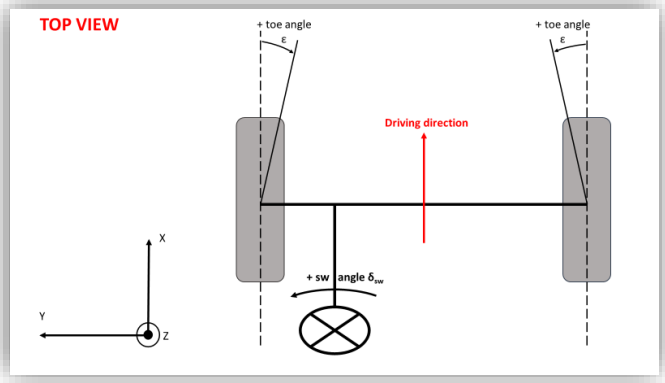

The steering ratio vs steering wheel angle map includes the kinematics and compliances of the steering and suspension systems and must be identified for the proper vehicle speed.

Axle characteristics

The axles characteristics can be computed by collecting, from the multibody simulations, the side slip angle α and lateral force F_y of the two axles in a ramp steer test. These maps are used in the models with variable cornering stiffness (Model 3-4).
The axle lateral forces are computed as the sum of the transversal components of the tire forces:

$$\begin{cases} F_{y,f} = F_{y,FL}\cos\delta_{w,FL} + F_{y,FR}\cos\delta_{w,FR} \\ F_{y,r} = F_{y,RL} + F_{y,RR} \end{cases} \quad (22)$$

Where:

$\boldsymbol{\delta_{w,FL}}$, $\boldsymbol{\delta_{w,FR}}$	Steer angles of the front left wheel and the front right wheel respectively

While the side slip angle of the axle is calculated as the mean value of the side slip angles of the two wheels on that axle:

$$\begin{cases} \alpha_f = \frac{\alpha_{FL}+\alpha_{FR}}{2} \\ \alpha_r = \frac{\alpha_{RL}+\alpha_{RR}}{2} \end{cases} \quad (23)$$

FIGURE 8 Characteristics of the front and rear axles (estimated vs real)

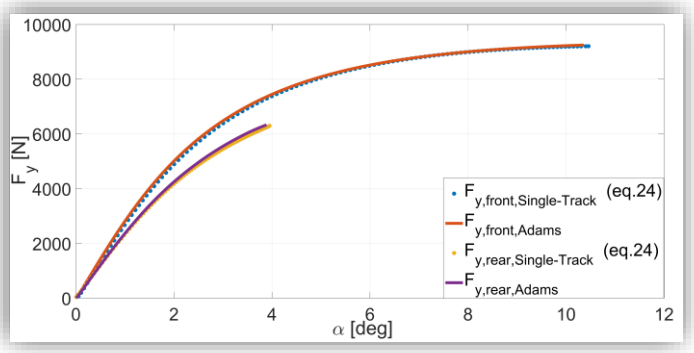

FIGURE 9 Cornering stiffness characteristic: direct derivative vs magic formula interpolation

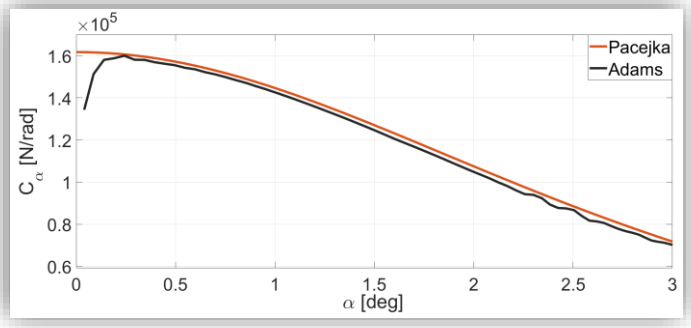

In the absence of a direct measurement of the lateral forces and side slip angles of each tire, the single track formulation can be used to estimate the F_y and α by knowing the kinematic quantities that are normally available during vehicle handling tests, e.g. from an inertial measurement unit and a side slip angle sensor or estimator:

$$\begin{cases} F_{y,f} = \frac{bma_y + J_z\ddot{\psi}}{L} \\ F_{y,r} = \frac{ama_y - J_z\ddot{\psi}}{L} \end{cases} \quad \begin{cases} \alpha_f = \delta_f - \beta - \frac{a}{u}\dot{\psi} \\ \alpha_r = -\beta + \frac{b}{u}\dot{\psi} \end{cases} \quad (24)$$

Hence, the axle characteristics can be obtained from the signals β, a_y and $\dot{\psi}$ in addition to the steer angle of the front wheels δ_f.
Figure 8 shows the good match between the characteristics of the axles obtained through the application of eq. 24 and the ones derived from the direct evaluation of (F_y, α) values from the multibody simulation.
One of the main limits of the classical single track model is the assumption of constant cornering stiffness. From Figure 9 it is possible to see that the cornering stiffness, which is the slope of the axle characteristic, is a monotonically decreasing function of the side slip angle. The cornering stiffness is defined as the derivative of the previous axle characteristic:

$$C_\alpha = \frac{dF_y}{d\alpha} \quad (25)$$

Furthermore, it is desirable to have a mathematical expression for the axle characteristic in order to avoid issues due to computation of numerical derivative of non-smooth simulation data and to have better result of cornering stiffness at low lateral acceleration, i.e. when the ramp steer starts to increase the steering wheel angle from zero. Therefore, the Pacejka's magic formula was introduced for the interpolation of the two axles characteristics:

$$\begin{cases} F_{y,f,PAC} = D_f \sin\left(C_f\, atan\left(B_f\alpha_f - E_f\left(B_f\alpha_f - atan(B_f\alpha_f)\right)\right)\right) \\ F_{y,r,PAC} = D_r \sin\left(C_r\, atan\left(B_r\alpha_r - E_r\left(B_r\alpha_r - atan(B_r\alpha_r)\right)\right)\right) \end{cases} \quad (26)$$

From the MB simulation results, the coefficients B,C,D,E of the magic formula that best fit the force vs side slip angle characteristic of the axles can be identified. Figure 9 shows the advantage of using an analytical rather than a numerical approach to evaluate the cornering stiffness, especially at low lateral accelerations.

Tire relaxation lengths

In order to introduce the tire lag in model 3 and 4, the influence of the relaxation length on the vehicle system dynamics is investigated. For this purpose, the FRF $\frac{F_y}{\alpha}$ for both the multibody model and the model 3 with the relaxation length disabled has been compared. The acquisition of these maps has been performed from a sine sweep maneuver. The FRF of $\frac{F_y}{\alpha}$ has been obtained through an estimation of the transfer function correlating the two signals. Assuming constant relaxation lengths, their influence on the vehicle dynamics acts as a

first order system [9] with a delay τ that depends on the vehicle velocity, such as:

$$\tau = \frac{d}{u} \tag{27}$$

Hence, the transfer function associated with the relaxation length model has the following expression in the Laplace domain:

$$G(s) = \frac{F_y}{F_{y,SS}} = \frac{1}{\tau s + 1} \tag{28}$$

Figure 10 shows the comparison between the FRF $\frac{F_y}{\alpha}$ between the multibody simulation and the one obtained through model 3 with no relaxation length. The ratio between these two curves defines the FRF response associated to the relaxation lengths (red markers in Figure 11). In Figure 11, these red markers are compared to the curves obtained by the description of the axle delay through a first-order constant relaxation length model (eq. 28). Hence, in model 2-3 and 4 the following relaxation lengths are identified for the default vehicle setup and maneuver specifications:

TABLE 3 Axles relaxation lengths

d_f[m]	0.48
d_r[m]	0.42

FIGURE 10 FRF Cornering stiffness

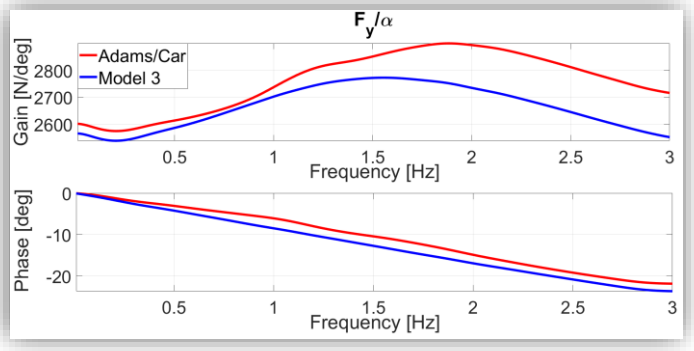

FIGURE 11 Comparison between the influence of relaxation length in Adams/Car with respect the modelled one

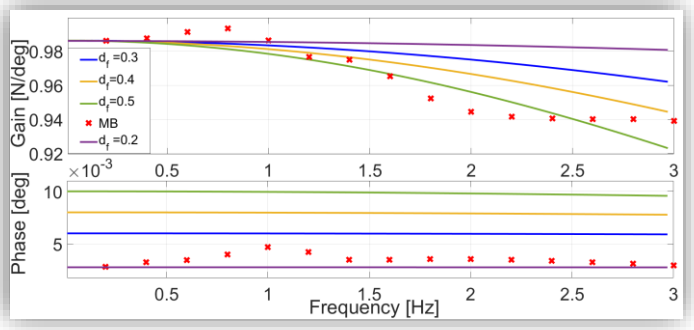

FIGURE 12 Relaxation length at different vertical load

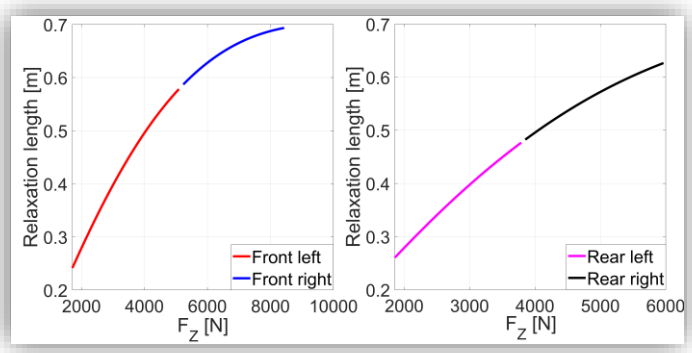

The tire relaxation length, as explained by Pacejka in [10], depends on the vertical load and camber angle. The equation used by the MB simulator is here reported:

$$\sigma_\alpha = P_{T_{y1}} \sin\left[2\, atan\left(\frac{F_z}{P_{T_{y2}} F_{z0} \lambda_{F_{z0}}}\right)\right](1 - P_{K_{y3}}|\gamma_y|) R_0 \lambda_{\sigma_\alpha} \lambda_{F_{z0}} \tag{29}$$

Where:

σ_α	lateral relaxation length
$P_{T_{y1}}$	peak value of relaxation length $\sigma_{\alpha 0}/R_0$
$P_{T_{y2}}$	value of $\frac{F_z}{F_{z0}}$ where σ_α is extreme
F_z	vertical load
F_{z0}	nominal wheel load
$P_{K_{y3}}$	influence of camber angle
γ_y	camber angle
R_0	free tire radius
λ_{σ_α} , $\lambda_{F_{z0}}$	scaling factors

The numerical values of the parameters in the former equation are taken from the property file of the tire model used for the multibody simulation. Figure 12 shows the relaxation length computed using the equation 29 in a ramp steer simulation of the multibody model. Hence, there are different values of vertical load and camber angle, that lead to a variable relaxation length during a ramp maneuver. In Figure 13 the relaxation lengths of each wheel at different sideslip angles are shown. This trend is used to identify the maximum and minimum value of the relaxation lengths to be used for the axles.

FIGURE 13 Relaxation length for each wheel at different slip angles

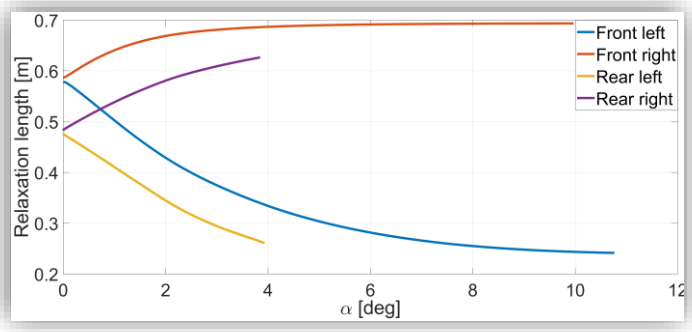

FIGURE 14 Anti-Roll Bar scheme

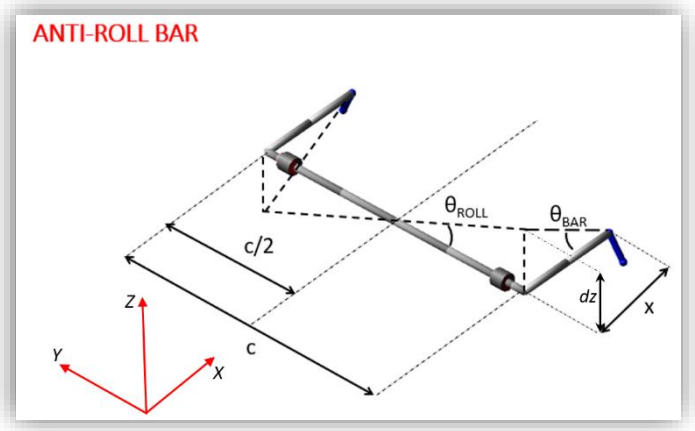

Roll stiffness and damping

Model 4 requires the estimation of two additional parameters that are roll stiffness and roll damping. The single contributions to the total roll stiffness include the front and the rear springs stiffness, the front and the rear antiroll bars and the chassis torsional stiffness. The multibody model under study is characterized by a rigid chassis, so the roll stiffness of the vehicle can be computed summing the contributions of the front and the rear suspension, because they can be considered as springs working in parallel. The hypothesis that front and rear springs are parallel to z axis can be applied in the considered case study. In fact, they are mounted concentric to the dampers and with very low inclination angles.

The following equations have been used to evaluate the total roll stiffness K_{ROLL}:

$$K_{ROLL} = K_{ROLL_{front}} + K_{ROLL_{rear}} \tag{30}$$

$$\begin{cases} K_{ROLL_{Front}} = K_{ROLL,spr,F} + K_{ROLL,ARB,F} \\ K_{ROLL,REAR} = K_{ROLL,spr,R} + K_{ROLL,ARB,R} \end{cases} \tag{31}$$

In order to compute the roll stiffness contribution due to the springs mounted on an axle, the following equation is used:

$$K_{ROLL,spr} = K_{spring} \frac{d_{SPRING}^2}{2} \tag{32}$$

K_{spring} is the spring stiffness and can be taken directly from the property file of the spring in the multibody model; d_{SPRING} is the lateral distance between springs, measurable from the design position (hardpoints) of the springs.
Concerning the roll stiffness contribution due to ARB, a further step is necessary, because the multibody software shows the torsional stiffness of the bar, and not directly the roll stiffness. Generally, the torsional stiffness of a solid bar with circular section can be computed as follows:

$$K_{TOR,BAR} = \frac{GI_P}{c} = \frac{G\frac{\pi d_b^4}{32}}{c} \tag{33}$$

where:

G	shear modulus
I_P	polar area moment of inertia
c	torsion bar length
d_b	torsion bar diameter

Considering the relationship between the involved angles and the roll moment equilibrium (Figure 14):

$$\theta_{ROLL} \frac{c}{2} = \theta_{BAR}\, x = dz \tag{34}$$

$$K_{ROLL,BAR}\, \theta_{ROLL} = 2 \frac{K_{TOR,BAR}\theta_{BAR}}{x} \frac{c}{2} \tag{35}$$

Combining these 2 equations, $K_{ROLL,BAR}$ can be computed:

$$K_{ROLL,BAR} = K_{TOR,BAR} \frac{c^2}{2x^2} \tag{36}$$

where:

θ_{ROLL}	Vehicle body roll angle
x	Arm length
θ_{BAR}	Arm angle, twist angle of the bar
$K_{ROLL,BAR}$	Roll stiffness due to ARB
$K_{TOR,BAR}$	ARB torsional stiffness
dz	Vertical displacement

The roll damping contribution due to shock absorbers is computed as follows:

$$C_{ROLL} = C_{ROLL\ SUSP,F} + C_{ROLL\ SUSP,R} \tag{37}$$

$$C_{ROLL\ SUSP} = C_{DAMPER} \cdot \frac{d_{DAMPER}^{\ 2}}{2} \tag{38}$$

where:

C_{ROLL}	Total roll damping
C_{DAMPER}	Damper damping coefficient
d_{DAMPER}	Lateral distance between shock absorbers

FIGURE 15 Damper characteristic and equivalent viscous damping (top), damper working points on a force vs displacement plane at different frequencies (bottom)

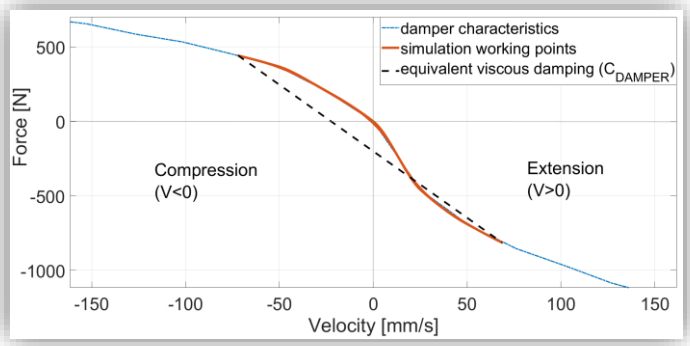

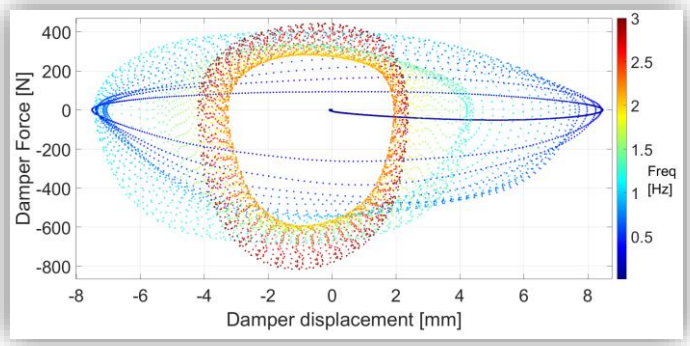

In order to evaluate the equivalent damping coefficient (C_{DAMPER}) the damper working points are analyzed during a sine sweep simulation. In the graph on the top of Figure 15, the damper characteristic (blue line) and the damper working points (red line) are shown. In order to identify a constant equivalent damping coefficient, the characteristic curve has been linearized by means of a line passing through the points corresponding to the maximum and minimum velocity that occurred during the simulation. The slope of this linearized characteristic represents the equivalent viscous damping coefficient of the shock absorber. In the bottom graph, the variation of the force at different damper displacement during the same sine sweep simulation is displayed. Moreover, the influence of the excitation frequency on the shape and size of the hysteresis cycles is illustrated.
In Table 4 the roll stiffness and damping calculated using equations 30-38 are shown.

TABLE 4 Roll stiffness and damping

$k_\phi \left[\frac{Nm}{rad}\right]$	155000
$c_\phi \left[\frac{Nms}{rad}\right]$	6182

These values of roll stiffness and damping applied to ST model 4 were verified via proper steady-state and frequency analysis. A ramp steer maneuver was carried out in order to validate the roll stiffness: the correlation index associated to the roll angle of ST model 4 with respect to MB model was evaluated. Then, a sine sweep maneuver was carried out in order to validate the roll damping through the comparison of the FRF of roll angle, velocity and acceleration obtained from ST model 4 with respect to the MB one.

FIGURE 16 Roll angle comparison between ST model 4 and MB model

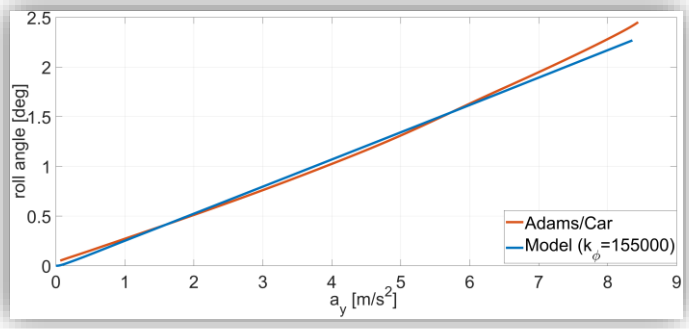

FIGURE 17 FRF correlation index between the ST model and the MB model at different roll damping

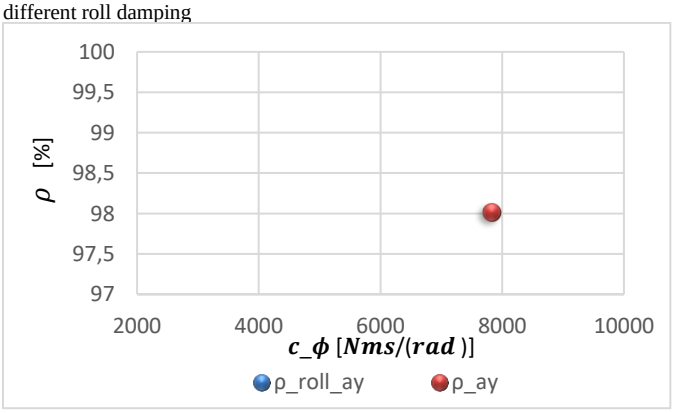

Figure 16 shows the steady state validation of the roll angle vs lateral acceleration by comparing ST model 4 and the MB model. In Figure 17 the comparison of the correlation index for different roll damping in transient conditions is shown. This picture illustrates the correlation index regarding the FRF *lateral acceleration / wheel steer angle* (red dots) and the FRF *roll acceleration / wheel steer angle* (blue dots) considering different roll damping. The lateral acceleration frequency response of the model gets high correlation with the multibody one, while the correlation of the roll acceleration FRF is much more influenced by the selection of the roll damping value. The best correlation is achieved with the nominal damping value computed as explained above. The FRFs β/δ and $\dot{\psi}/\delta$ do not exhibit significant variations for different roll damping. Therefore, eq. 30-38 give proper value of roll stiffness and damping.

Results and Discussion

In this section the comparison between the multibody results and the various single track models is shown both in steady-state and during transients. The steady-state analysis is done through Ramp steer simulations at constant vehicle speed and with a linearly increasing steering wheel angle. During this analysis, the understeer and side-slip angle gradients characteristics as a function of lateral acceleration are compared between the models by computing the root-mean-square (RMS) of the estimation error. The transient analysis is carried out through sine sweep steering maneuvers at constant vehicle speed; the comparison between the models is given by evaluating the correlation index of the typical FRF used in handling analysis, i.e. $\boldsymbol{a_y/\delta_f}$, $\boldsymbol{\beta/\delta_f}$ and $\boldsymbol{\dot{\psi}/\delta_f}$. Finally, a sensitivity analysis is carried out to show which and how the equivalent parameters/maps of the single track models change according to modified working condition of the reference multibody car model.

Steady – State Analysis

A ramp steer at constant vehicle speed with an increasing steering wheel angle of 10 $\frac{^\circ}{s}$ rate is simulated and the vehicle response in terms of understeer gradient and vehicle side-slip angle gradient vs lateral acceleration is plotted in Figure 18 and 19 for the different models. Model 2 in steady-state behaves exactly as the Model 1 therefore it is not reported in the charts.

FIGURE 18 Comparison of understeer gradient characteristics between ST model 4 and multibody

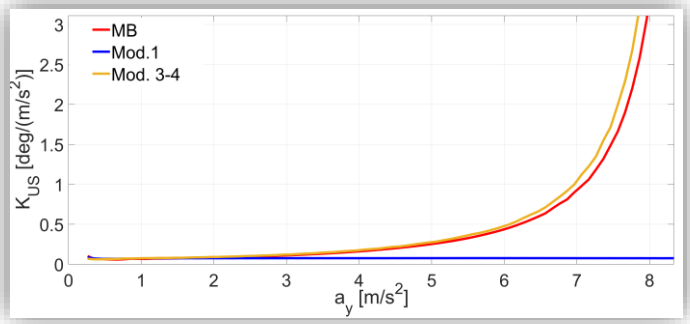

FIGURE 19 Comparison of vehicle side-slip angle gradient characteristics between single track model 4 and multibody

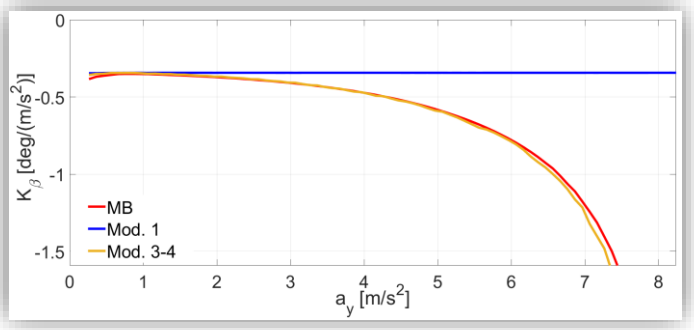

FIGURE 20 RMS error of the understeer and side-slip angle gradient maps for the model 1, 3 and 4 considering the multibody results as reference.

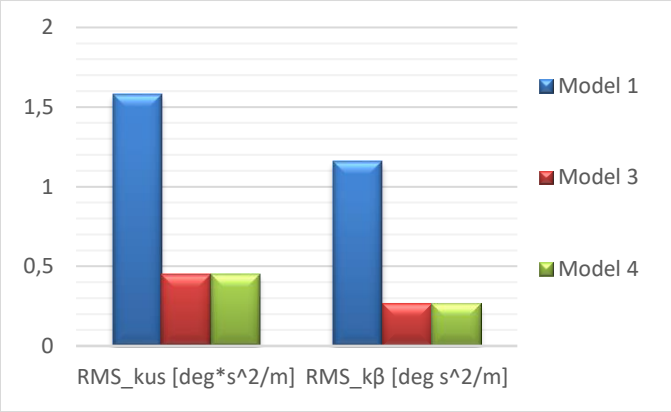

It is important to underline that the parameters and maps of each ST model must be evaluated and updated for each specific maneuver (e.g. for different vehicle speed or steering wheel input) and vehicle configuration.

Firstly, the trends of the two gradients (see Figure 18 and 19) for the linear single track model (Model 1), show a good match with the multibody one up to 2-3 $\frac{m}{s^2}$, i.e. until the car behaves almost linearly. By introducing the variation of axle cornering stiffness with side-slip angle, the understeer gradient characteristic approaches the multibody one with an accuracy increase of 70%.

The differences between the models has been quantified by means of the rms error, which is defined as follows:

$$RMS_{error} = \sqrt{\frac{1}{N}\sum_{i=1}^{N}\left(y_{model,i} - y_{multibody,i}\right)^2} \quad (39)$$

In Figure 20 the rms of the estimation errors for model 1, 3 and 4 are reported. In steady-state the most important contribution is given by the introduction of variable cornering stiffness (~70%), while the introduction of the roll motion does not provide any enhancements.

FIGURE 21 FRF comparison between all the ST models and the multibody

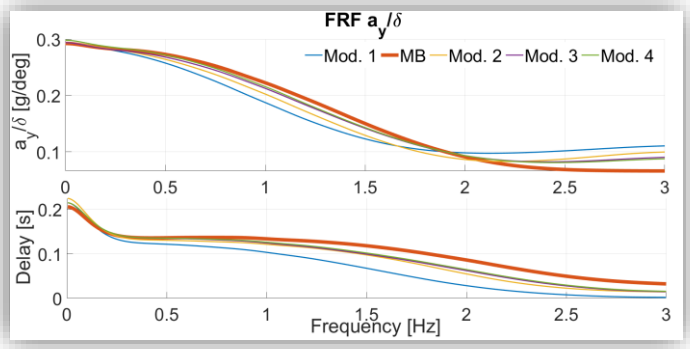

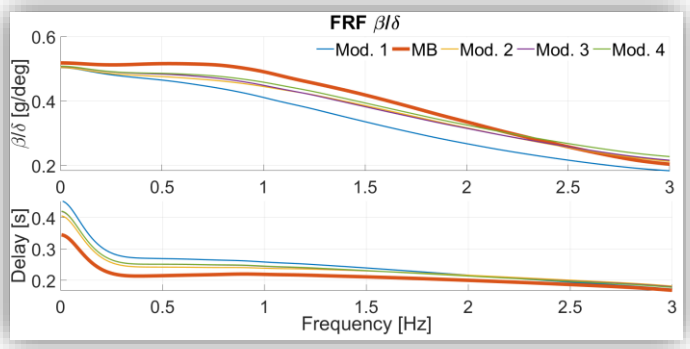

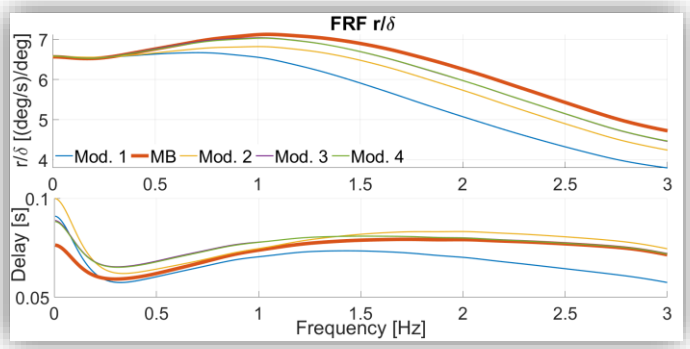

Anyway, model 4 permits the roll angle evaluation that is not feasible with the other models, see e.g. Figure 16 where the comparison of the roll angle obtained through model 4 with respect the multibody result is reported ($\boldsymbol{RMS_{error} = 0.105\ deg}$).

Frequency analysis

In this section, the FRFs of a_y/δ, β/δ and $\dot{\psi}/\delta$ related to the different models are shown. A sine sweep steering maneuver (-40,40)° at 90 $\frac{km}{h}$ is launched for the different models to evaluate their transient response. In Figure 21 the frequency responses, in terms of magnitude and delay, are compared. The introduction of axle relaxation length (Model 2), variable cornering stiffness (Model 3) and roll motion (Model 4) progressively move all the ST curves closer to the multibody ones. In order to do a reliable evaluation of the correlation between the multibody and the ST models, both magnitude and phase of the FRFs have been considered. In particular, the proposed correlation index for FRF evaluation is the arithmetic mean of the correlation of the magnitude and the delay of each FRF:

$$\rho = mean(\rho_{magnitude}, \rho_{delay}) \quad (40)$$

Using the mathematical expression of the correlation index (*eq. 20*), it is possible to compare the ST models with respect to the multibody one (Figure 22). This radar plot shows that the relaxation lengths is one of the most important parameters that must be included in simplified vehicle modelling for a proper estimation of the frequency response. Another improvement in terms of lateral acceleration and yaw rate is achieved introducing variable cornering stiffness.

FIGURE 22 Correlation index for the different models at 90 km/h

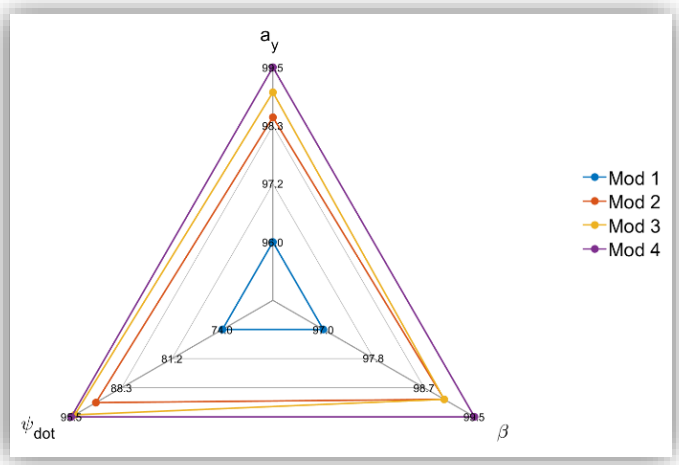

FIGURE 23 Correlation increase (in percentage) of the ST models with respect to Model 1.

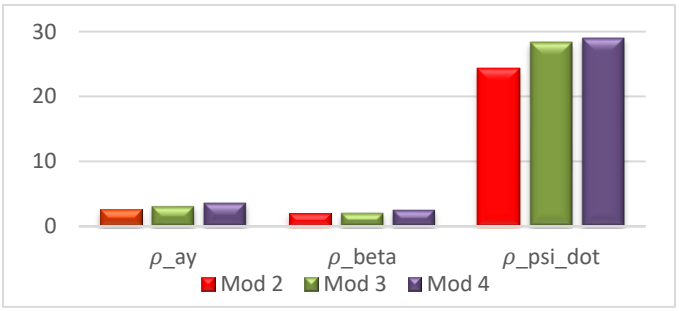

Finally, the introduction of roll provides a further improvement in estimating the lateral acceleration and vehicle side-slip angle. To better highlight the effect of the characteristics of the ST model on the individual FRFs, a bar graph of the percentage increase in correlation passing from Model 1 to the others is shown in Figure 23.

Parameter Sensitivity Analysis

In this section, the authors want to highlight the capability of the ST models, if properly initialized, to match the MB simulations results when the test conditions or some vehicle characteristics change. Moreover, the methodology to estimate the maps and parameters required by the ST models will be presented.

Vehicle speed

The handling performance of the vehicle was simulated at two longitudinal speeds of 90 and 130 $\frac{km}{h}$.

The first step of the proposed methodology is the identification of the unknown parameters and maps of the ST models. By processing the simulation results of the MB model the axle characteristics and the steering ratio map are extracted, as shown in Figure 24. It can be noted that: the lateral force characteristics of the axles are not sensitive to the considered variation of the vehicle speed, while the steering ratio gets higher values for small steering wheel angles. No differences in roll stiffness and damping were observed between 90 e 130 km/h, while a dedicated analysis must be done for the relaxation lengths.

FIGURE 24 Steering ratio (top) and axles cornering force (bottom) maps for two vehicle speeds

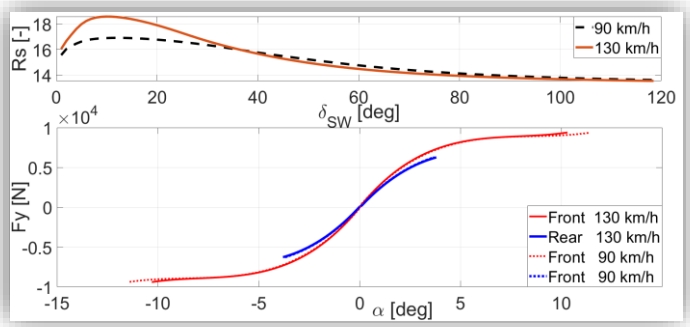

FIGURE 25 Relaxation length identification for the rear axle

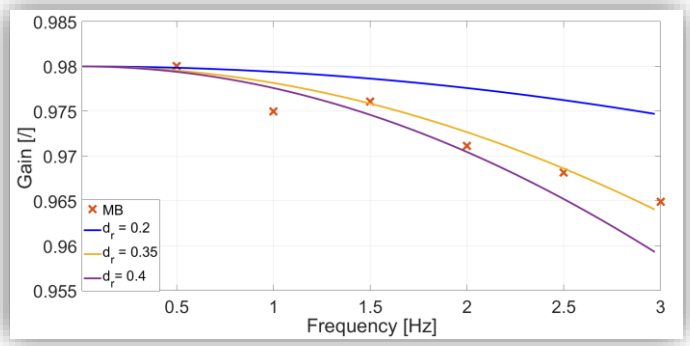

As explained in "Methodology" section, from the comparison of the MB tire dynamics (red markers) and the constant relaxation length tire model (Figure 25) it is possible to estimate a value for an equivalent relaxation length of the axles. The results of the parameter estimation are here reported:

d_f[m]	0.45
d_r[m]	0.35

After the parameter estimation, a ramp steer maneuver at 130 $\frac{km}{h}$ has been carried out. In Figure 26 the understeer characteristic is shown for the two velocities. In the considered speed range (90-130km/h) the understeer curve is not sensitive to speed change up to $a_y = 7\ m/s^2$, while for higher lateral accelerations a higher vehicle speed provokes a backward shift of the vertical asymptote. This trend is confirmed by both MB and ST models. Then, a sine sweep maneuver was computed. The correlation index for the different FRFs still remains high at 130 km/h. As an example, in Figure 27 the effect of the vehicle speed on the FRF of the lateral acceleration is shown. The ST model shows a very high correlation with the MB one.

FIGURE 26 Understeer characteristics at 90 and 130 km/h

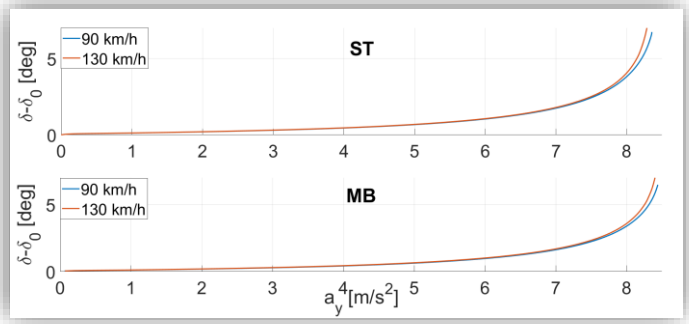

FIGURE 27 Effect of the vehicle speed on the FRF of lateral acceleration

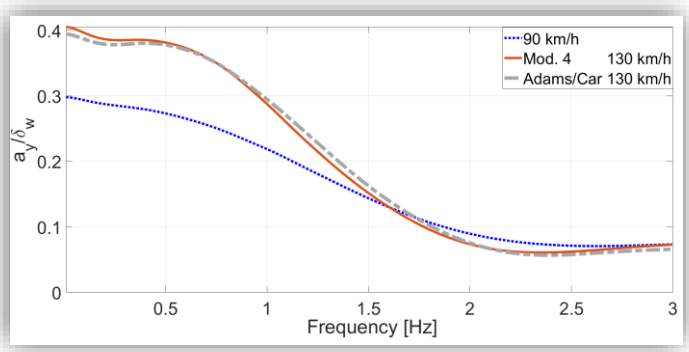

Vehicle Mass

As well as the velocity, vehicle mass has a significant impact on the model response too. Once again, it is necessary to identify the maps and parameters to be used in the ST model. From a ramp steer maneuver at 90 $\frac{km}{h}$ with an increased mass of 2155 kg the steering ratio (eq. 21) and the axle characteristics (eq. 24) are derived from Adams/Car data. As is shown in Figure 28, different steering-ratio and axle characteristics must be loaded to model the mass influence. The relaxation lengths are then identified by comparing the first order transfer function (eq. 28) with the axle dynamic behavior extracted from the simulations.

d_f[m]	0.62
d_r[m]	0.40

FIGURE 28 Understeer characteristics for different vehicle mass simulations

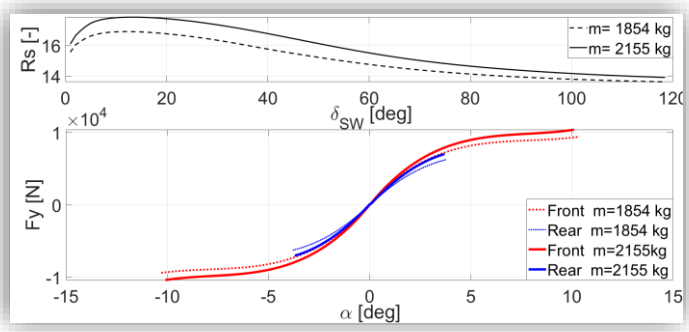

FIGURE 29 Relaxation length identification for different vehicle mass

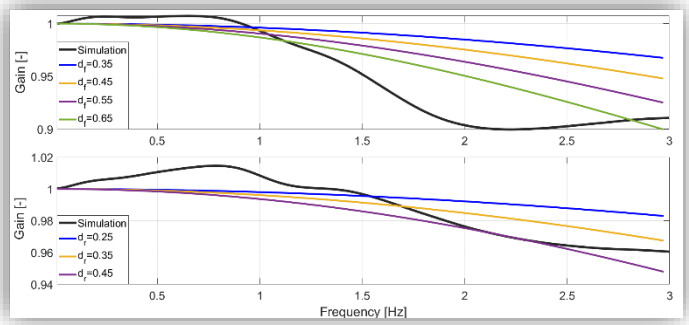

FIGURE 30 Effect of vehicle mass on the steady-state vehicle response.

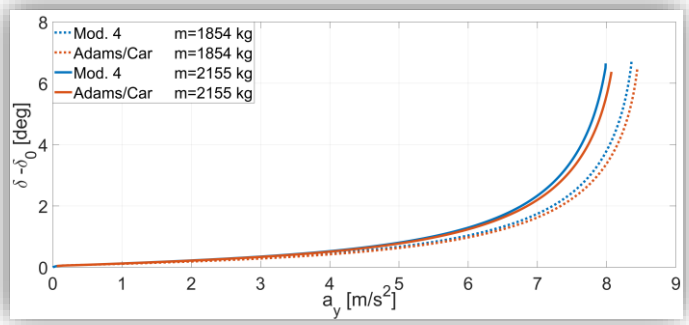

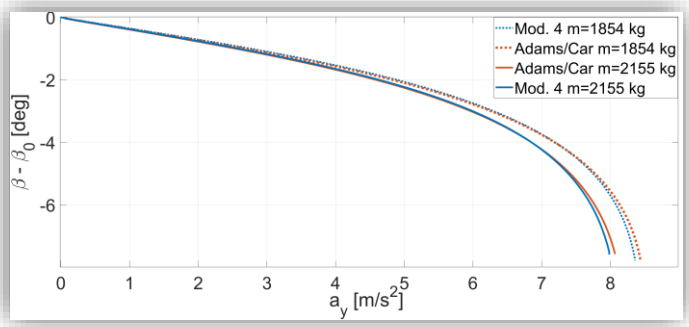

Then, a steady-state analysis has been computed. In Figure 30 the comparison of the understeer and vehicle side-slip angle characteristics at different mass is illustrated. A 16% increase in vehicle mass without changing the COG position increases the understeer tendency of the car and reduces the maximum lateral acceleration. Finally, a sine sweep maneuver has been computed to evaluate the effect on the transient performance of the car.

FIGURE 31 Effect of vehicle mass on the main FRFs

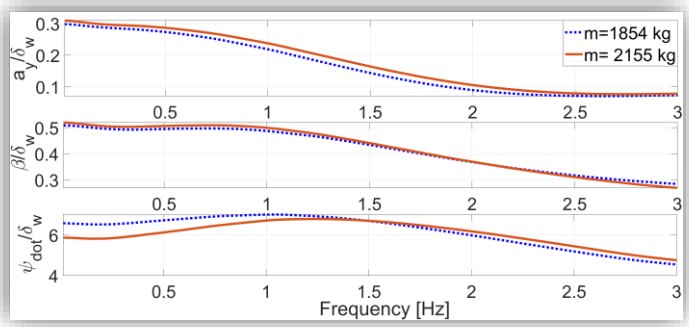

The correlation index for the different FRFs still remains high.

$$\rho_{ay} = 95\%; \rho_{\beta} = 99.5\%; \rho_{\psi_{dot}} = 98\%$$

In the Figure 31 the different frequency response functions are shown, the mass influence is higher for $\frac{\dot{\psi}}{\delta}$ FRF, where the increase of vehicle mass determines a significant reduction of the magnitude in the low frequency range.

Toe angles

A suspension parameter that can be tuned to condition the vehicle cornering behavior is the static toe angle. In this section a static toe angle is imposed at the front wheels of the car and its effect on vehicle lateral dynamic is analyzed.

The parameter estimation method for a vehicle with static toe angles is illustrated. Starting from the MB simulation results of a ramp steer test at the required vehicle speed, derive the steady-state characteristics of the steering ratio and the axles lateral forces. In Figure 32 the variations of the maps are shown. More in detail, the steering ratio increases for positive toe angles (toe-in) while it reduces for negative toe angles (toe-out).

FIGURE 32 Maps for different toe angles

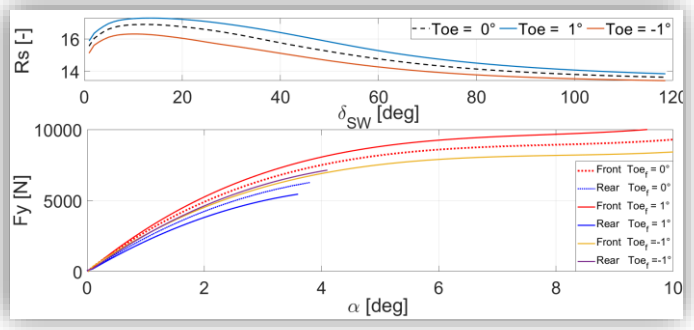

FIGURE 33 Relaxation lengths identification for front wheel toe angle of 1°

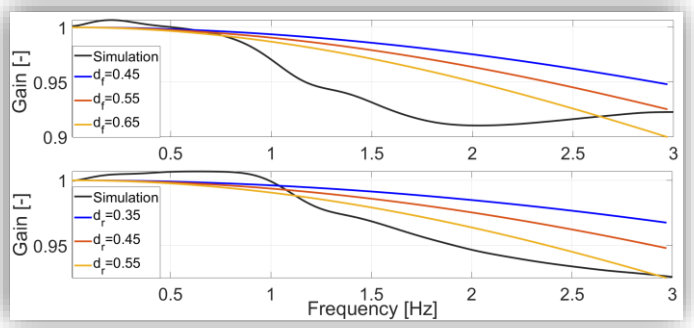

The axle cornering stiffness increases as the toe angle increases on the same axle, while the cornering stiffness of the second axle reduces. Then, it is necessary to identify the values of the front and rear relaxation lengths. In Figure 33 the analysis of the relaxation length for the rear axle regarding the simulation with 1° of toe angle on the front wheels is shown.

d_f[m]	0.65	TOE_front 1°
d_r[m]	0.55	
d_f[m]	0.82	TOE_front -1°
d_r[m]	0.59	

In Figure 34 the comparison of the understeer characteristics at different toe angles is illustrated.

FIGURE 34 Effect of front wheel toe angle on the steady-state vehicle response

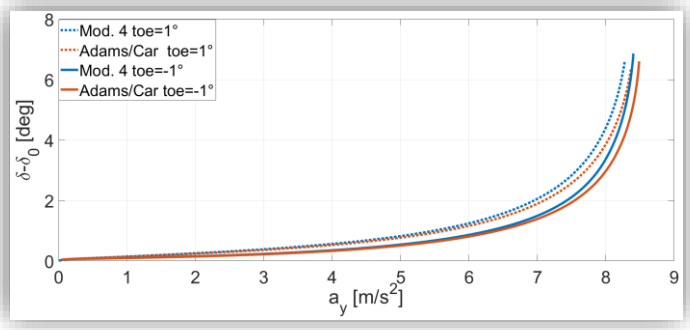

FIGURE 35 Effect of front wheels toe angle on the FRFs

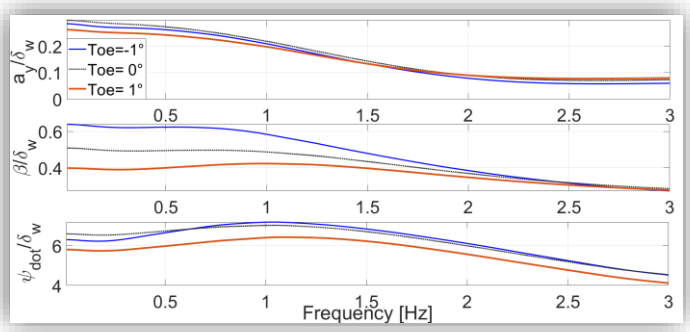

The correlation index analysis applied to the transient simulation results shows that the different FRFs are very well predicted even when the toe angles (and the corresponding maps and parameters) are changed:

$$\rho_{ay} = 95.5\%; \rho_{\beta} = 99.5\%; \rho_{\psi_{dot}} = 98\% \quad for\ toe = +1°$$
$$\rho_{ay} = 94\%; \rho_{\beta} = 99\%; \rho_{\psi_{dot}} = 97.8\% \quad for\ toe = -1°$$

In Figure 35 the different responses are shown for the ST model only. The dynamic effect of toe-in on the front wheels is to reduce the responsiveness of the steering, as can be seen in the understeer plot, and improve stability ad high speeds, as evidenced by the side slip angle FRF.

Anti-roll bar stiffness

Stiffness of anti-roll bars also has a strong influence on the handling performance of a car. In this section, two different configurations, with nominal and triplicated stiffness of the rear anti-roll bar are shown. The parameters estimation for the two considered vehicle setups, characterized by different anti-roll bar stiffness, was performed. It came up that steering ratio is not influenced by the increment of anti-roll bar torsional stiffness, while the axle characteristics show noticeably different trends (see Figure 36).

FIGURE 36 Steady-State maps for different anti-roll bar stiffness

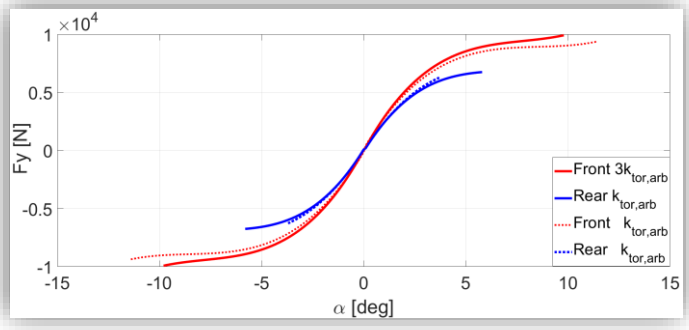

FIGURE 37 Steady-state simulation for different $k_{tor,arb}$

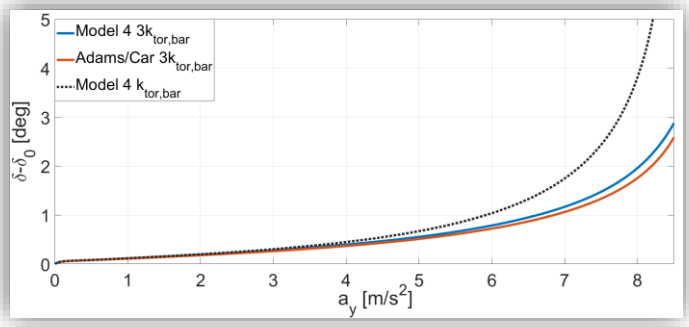

FIGURE 38 Frequency simulation for different $k_{tor,arb}$

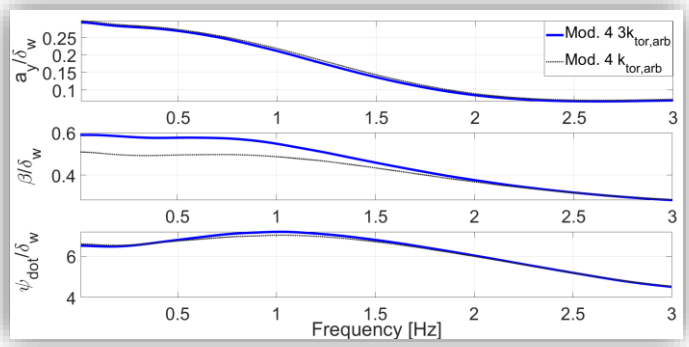

A result of the steady state analysis is shown in Figure 37, where the comparison of understeer characteristics obtained with different anti-roll bar stiffness is illustrated. Increasing rear anti-roll bar stiffness reduces the vehicle understeer.
The results of transient analysis are reported in Figure 38, where the different frequency response functions are shown for the two vehicle setups. The roll stiffness distribution among the axles highly influences the FRF $\frac{\beta}{\delta}$ while it has less influence on the other transient responses. The correlation index for the different FRFs still remain high throughout the sensitivity.

Center of Gravity position

Another aspect that was investigated is the sensitivity to the longitudinal position of vehicle center of gravity for the same value of total vehicle mass. The results of the parameters estimation and the change in vehicle handling behavior are illustrated.

FIGURE 39 Steady-State maps for different COG longitudinal positions

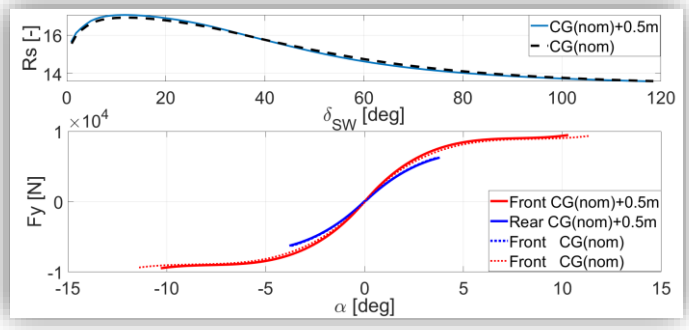

FIGURE 40 Understeer curves for different COG longitudinal positions

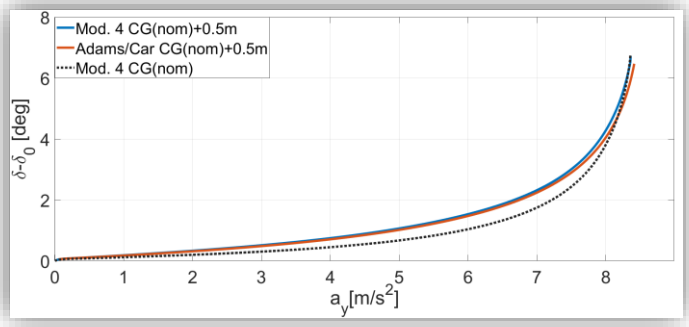

FIGURE 41 Frequency analysis for different COG longitudinal positions

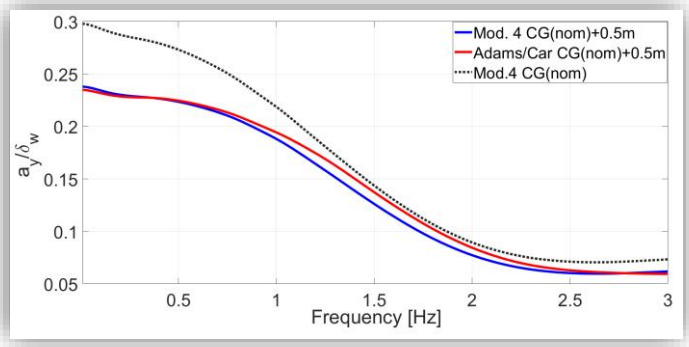

The steering ratio is very small influenced by moving the center of gravity to the front axle, while the axle characteristics show an increase of the cornering stiffness on the axle where the weight is moved, i.e. the front in the analyzed case, and a reduction on the other one.
In Figure 40 the comparison of the understeer characteristics for the considered COG positions is illustrated. By moving the COG toward the front axle, the vehicle shows more understeer. As for the frequency sweep, the correlation index for the different FRFs still remains high. In Figure 41 $\frac{a_y}{\delta}$ FRF is shown: shifting the COG towards the front axle led to a reduction in the lateral acceleration gain in the low frequency range.

Conclusion

This work presented four single track models with increasing complexity and investigated their correlation with respect to a multibody model used as reference, in terms of vehicle lateral dynamics response. The main conclusions are:

1. The introduction of a tire delayed response through the relaxation length, the nonlinearity in the axles steady-state

cornering behavior and the roll dynamics effect clearly shows an improvement with respect to the classic two degrees of freedom single track model with constant parameters (Model 1): the main contribution to the steady-state response correlation is provided by the introduction of lateral forces with variable cornering stiffness (Model 3 and Model 4) thus achieving an improvements of 70% in terms of understeering characteristics RMS errors. The effect of the relaxation length (Model 2) is greatly appreciated from the frequency response functions especially for the phase delay correlation with respect to the Model 1. The variable cornering stiffness introduced by Model 3 and Model 4 also provide a further improvement to the FRF response magnitude.

2. The methodology used for extracting the parameters/maps of the four single track models from the multibody model represents a novel contribution point achieved by this activity. It can be also applied and extended to experimental applications where all required measurements are available for the parameters estimation procedure. The procedure and the correlation results show the importance of evaluating a proper steering ratio characteristic, as well as axles nonlinear steady-state cornering stiffness, to include the effect of suspensions kinematics and compliances on cornering responses.

3. The concept of the tire delay response as a first order dynamic model, can be extended to the axle transient response by introducing an equivalent axle relaxation length as it is conventionally adopted for the individual tire model.

4. The sensitivity analysis conducted on the Model 4 against the vehicle speed, the vehicle overall mass, the toe angle, the anti-roll bar stiffness and the center of gravity position clearly proved the model robustness in terms of steady-state and transient responses correlation when parameters are updated according to the methodology described in this paper.

References

1. Galvagno, E., Galfrè, M., Velardocchia, M., Morello, A. et al., *Experimental-Numerical Correlation of a Multibody Model for Comfort Analysis of a Heavy Truck*, SAE Technical Paper 2020-01-0768, 2020, https://doi.org/10.4271/2020-01-0768

2. Mavros, G.: *A study on the influences of tyre lags and suspension damping on the instantaneous response of a vehicle*. Proc. Inst. Mech. Eng. Part D J. Autom. Eng. 222 (4), 485-498 (2008)

3. Mosconi L., Farroni F., Sakhnevych A., Timpone F., Capobianco A., Gerbino F.S. (2021). *Identification of Tire Transient Parameters from Vehicle Onboard Sensors Data*. In: Niola V., Gasparetto A. (eds) Advances in Italian Mechanism Science. IFToMM ITALY 2020. Mechanisms and Machine Science, vol 91.

4. M. Guiggiani. (2018). *The Science of Vehicle Dynamics* (2nd ed.). Springer.

5. International Organization for Standardization, ISO 4138:2004, "*Passenger cars – Steady-state circular driving behavior – Open-loop test method* ", International Organization for Standardization (2004).

6. Galvagno, E., Mauro, S., Pastorelli, S., Servetti, A., & Tota, A. (2020). *A Smart Measuring System for Vehicle Dynamics Testing* (No. 2020-01-1066). SAE Technical Paper.

7. Selmanaj, D., Corno, M., Panzani, G., & Savaresi, S. M. (2017). Robust vehicle sideslip estimation based on kinematic considerations. *IFAC-PapersOnLine*, *50*(1), 14855-14860.

8. International Organization for Standardization, ISO 7401:2003, "*Road vehicles – Lateral transient response test methods – Open-loop test method* ", International Organization for Standardization (2003).

9. R. Bracewell. (1999). *The Fourier Transform & Its Applications* (3rd ed.). Stanford, CT: McGraw-Hill.

10. ADAMS/Tire Manual, 2005, MSC Software Corporation.

11. Ozer DJ. Correlation and the coefficient of determination. Psychol Bull. 1985;97:307–315.